Journal of Alloys and Compounds 1037 (2025) 182400

Contents lists available at ScienceDirect

Journal of Alloys and Compounds

journal homepage: www.elsevier.com/locate/jalcom

α-$LiFe_5O_8$ as the cathode of a supercapacitor integrated in a three-electrode photo-supercapacitor

J.J. Peinado-Pérez [b], F. Martín [a], M.C. López-Escalante [a,*]

[a] Departamento de Ingeniería Química, Facultad de Ciencias, Universidad de Málaga, Málaga 29071, Spain
[b] Departamento de Física Aplicada I, Facultad de Ciencias, Universidad de Málaga, Málaga 29071, Spain

ARTICLE INFO

Keywords:
Electrolyte nature
Supercapacitor
Photo-supercapacitor
Indoor environment

ABSTRACT

This study investigates the use of lithium ferrite α-$LiFe_5O_8$ (LFO) thin film electrodes as cathodes in both asymmetric supercapacitors (ASC) and three-electrode photo-supercapacitors (PSC). The nature of the electrolyte plays a fundamental role in these systems. Therefore, LFO was characterised in a three-electrode electrochemical cell using two aqueous solutions: 0.5 M Na_2SO_4 and 0.5 M $LiClO_4$, yielding specific capacities of 119 and 70 F g^{-1}, respectively, at a current density of 0.5 A g^{-1}. LFO was then assembled in an ASC with a $ZnMn_2O_4$ electrode as the anode, and the influence of two different electrolytes was studied: an aqueous solution of 0.5 M Na_2SO_4 and a polymer gel containing polyvinyl pyrrolidone (PVP) and $LiCLO_4$. The ASCs exhibited distinct behaviour depending on the electrolyte used. The device response shifted from that of a pseudocapacitive supercapacitor (Na_2SO_4) to that of a hybrid supercapacitor (PVP–$LiClO_4$). ASC devices containing Na_2SO_4 or PVP–$LiClO_4$ electrolytes exhibited maximum specific capacitances of 52 and 64 F g^{-1}, respectively, at a current density of 0.5 A g^{-1}; the corresponding energy densities were 13 and 32 Wh kg^{-1}, power densities were 237 and 473 Wh kg^{-1}, and capacity retention were 20 % and 50 %, respectively. Three-electrode PSCs were prepared by integrating a dye-sensitised solar cell into the power generation system. The highest performances were obtained under low irradiance, with storage and overall efficiencies of 43.20 % and 1.46 %, respectively.

1. Introduction

The generation of electricity through solar photovoltaic energy is a safe and reliable process that has contributed to the democratisation of energy access and enhanced energy independence in many regions lacking fossil fuel resources or the economic means to acquire them [1,2]. To date, most research has focused on large-scale energy generation in outdoor environments, with energy storage receiving comparatively less attention. However, the increasing use of portable and remote consumer electronics has highlighted the need for versatile indoor-capable devices that can both generate and store electricity [3]. These devices, known as photo-supercapacitors (PSCs) or self-recharging supercapacitors (SCs), are typically designed using one of three architectures [4].

The first architecture combines two individual devices using an external circuit (four electrodes), resulting in a large, costly product with limited compatibility with other systems. The second uses a common intermediate electrode between the generation and storage units, producing a simplified three-electrode system. The third architecture uses photoelectrodes with both photoactive and capacitive properties, resulting in a simple but inefficient two-electrode system [5–7]. The reported overall and storage efficiencies of perovskite solar cells greatly depend on the technology implemented. For instance, Joselene Suzan et al. [2] reported a device integrating a dye-sensitised solar cell (DSSC) cell into an inline PSC with an overall efficiency of 8.98 %. In their review on perovskite-based PSCs, Rout et al. [7] reported overall efficiencies of 2.8 %–11.5 % and storage efficiencies of 73.77 %–92 %. However, these devices demonstrated low stability over time. For two-electrode PSCs, performance values are presented as capacitances derived from galvanostatic charge–discharge (GCD) tests. For example, Chauhan et al. [8] demonstrated a symmetrical PSC with ZnO–FTO electrodes achieving 18.26 mF cm^{-2} at a current density of 0.41 mA cm^{-2}.

In general, PSCs require the development of environmentally friendly, low-cost, and electrochemically compatible materials for photoelectrodes, storage electrodes, and electrolytes. Additionally, efforts must focus on material integration to improve the overall efficiency, stability, and reliability of PSCs, as well as the optimisation of

* Corresponding author.
E-mail address: mclopez@uma.es (M.C. López-Escalante).

https://doi.org/10.1016/j.jallcom.2025.182400
Received 8 April 2025; Received in revised form 17 July 2025; Accepted 19 July 2025
Available online 21 July 2025

the connections between components [9,10]. For generation units, a clear trend is observed towards the use of emerging photovoltaic technologies, especially organic [7], perovskite [11], and dye-sensitised technologies [12]. In terms of storage units, SCs employing various storage mechanisms—electric double-layer, pseudocapacitive, and hybrid—are of particular interest [13–16]. Regarding electrolytes, aqueous solutions are widely used due to their low toxicity [17], while polymer gels are also employed for their ease of handling [18].

To address these challenges, a three-electrode PSC has been developed, combining a DSSC with an asymmetric SC (ASC). DSSCs are known for their low cost, ease of fabrication, industrial transferability, and reasonable conversion efficiency for indoor energy charging [2,5,9]. The selected ASC consists of a $LiFe_5O_8$ (LFO) thin film cathode and a $ZnMn_2O_4$ (ZMO) anode in a tetragonal spinel form. LFOs are cubic ferrites with a spinel structure, exhibiting two crystalline phases, α and β. The ordered α-$LiFe_5O_8$ phase forms at low temperatures (440 °C) and has an inverted spinel-like structure where Li^+ and three-fifths of Fe^{3+} occupy octahedral sites, while the remaining Fe^{3+} occupy tetrahedral sites. The disordered β-$LiFe_5O_8$ phase occurs at temperatures above 730 °C and contains randomly distributed ions [19,20]. LFO is notable for its ferrimagnetic ordering and stable electronic structure across a broad temperature range, indicating good electronic conductivity and structural durability under cyclic operation, while also being cost-effective [19]. Among its various technological applications, its use as a battery electrode is particularly notable owing to its high capacity of 257 mAh g^{-1} at 28 mA g^{-1} [19].

The anode consists of tetragonal spinel ZMO. Manganese oxide-based materials are of interest for both SC and battery applications because of their high theoretical specific capacitance, excellent capacitive performance in aqueous electrolytes, multivalency, low cost, and environmental compatibility [21].

Regarding the electrolyte, this study investigates how electrolyte composition influences pseudocapacitive processes and electrode compatibility.

With these considerations, the behaviour of LFO electrodes prepared by spray pyrolysis was analysed across three configurations. In the first, the electrodes were tested in a three-electrode electrochemical cell using 0.5 M Na_2SO_4 and 0.5 M $LiClO_4$ to evaluate charge storage. In the second, LFO served as a cathode in an ASC to study the influence of the electrolyte—aqueous Na_2SO_4 or semi-solid polyvinyl pyrrolidone (PVP)–$LiClO_4$—on device performance. In the third, LFO was used as the storage electrode in a three-electrode PSC tested in both indoor and outdoor environments. The study demonstrates the versatility of the prepared material and the critical role of the electrolyte in energy storage devices with and without self-charging capability.

2. Materials and methods

2.1. Preparation of LFO and ZMO electrodes

Thin films of LFO and ZMO were prepared on a 2.5 × 4.0 cm commercial indium tin oxide (ITO; In_2O_3:Sn) glass substrate using the spray pyrolysis technique, following the same procedure for both materials. The LFO precursors, lithium acetate dihydrate ($C_2H_3LiO_2{\cdot}2\ H_2O$), and iron acetylacetonate ($C_{15}H_{21}FeO_6$), were dissolved in a mixture of double-distilled water, acetic acid, and isopropanol in a molar ratio of 1.33:2.0:1.0. The final concentration of Li^+ and Fe^{3+} was 0.04 M. Deposition by spray pyrolysis was conducted at 400 ºC for 2, 5, and 10 min.

For ZMO, the precursors, zinc acetate dihydrate ($C_4H_6O_4Zn{\cdot}2\ H_2O$) and manganese acetate tetrahydrate ($C_4H_6O_4Mn{\cdot}4\ H_2O$), were dissolved in double-distilled water to produce final concentrations of 0.005 M Zn^{2+} and 0.01 M Mn^{2+}. Deposition was performed for 2 min at 400 ºC [21].

2.2. SC assembly

ASCs were assembled using LFO and ZMO electrodes and two electrolytes with an approximate pH of 6. The first electrolyte, designated as El-Na_2SO_4, consisted of a 0.5 M Na_2SO_4 aqueous solution impregnated in an acetate film. The second, designated as El-PVP-$LiClO_4$, was a gel polymer electrolyte consisting of 1.0 g of $LiClO_4$ and 1.0 g of PVP (M_w: 1300,000) dissolved in 12.5 mL of ethanol [21]. To prevent direct electrode contact and electrolyte loss, the ASCs were sealed at 60 ºC using a 25 Meltonix film frame (Solaronix).

2.3. Fabrication of DSSCs

A homemade DSSC served as the solar energy generation unit. The entire structure was prepared on a 4.0 × 1.0 cm commercial fluorine-doped tin oxide (FTO)/glass substrate. The electron transport layer consisted of a 34-nm-thick TiO_2 thin film deposited using magnetron sputtering (AJA International, Inc.) with a TiO_2 target (99.9 % pure; AJA International, Inc.) at 150 W, in a vacuum chamber under 3-mTorr Ar atmosphere. The deposition temperature and time were 300 ºC and 1 h, respectively.

A mesoporous TiO_2 film was screen-printed using a paste prepared from 6.0 g TiO_2 nanoparticles (P25, Degussa), 1.0 mL glacial acetic acid, and 135.0 mL ethanol, added dropwise under stirring until homogeneously mixed. Subsequently, 20.0 g terpineol and 3.0 g ethyl cellulose were added to the mixture and stirred until an appropriately consistent paste was obtained [22]. Finally, the photoelectrode was immersed in a 0.5-mM N-719 dye solution (Ossila) in ethanol for 24 h at room temperature.

The counter electrode comprised a Pt thin film deposited on a double-sided ITO glass substrate (4.0 × 2.5 cm) by magnetron sputtering for 30 s, along with an iodine/iodide redox couple.

2.4. PSC assembly

The prepared DSSC and ASC were assembled to form a PSC with a double-sided ITO-coated glass substrate as the intermediate electrode. The substrate was coated with a thin film of Pt on the DSSC-facing side and ZMO on the ASC-facing side. The assembly was completed with an LMO electrode and El-PVP-$LiClO_4$ as the electrolyte.

2.5. Characterisation methods

The crystallinity of the electrodes was assessed using an EMPYREAN X-ray diffractometer (PANanalytical; Malvern, UK). High-resolution transmission electron microscopy (HRTEM) and energy-dispersive X-ray spectroscopy (EDS) images were obtained using a Talos F200X (Thermo Fisher Scientific; Waltham, MA, USA). Electrode morphology was examined using a Helios Nanolab 650 dual-beam instrument (Thermo Fisher Scientific; Waltham, MA, USA) with a field emission scanning electron microscope (FESEM). Optical transmittance spectra were obtained using a Varian Cary 5000 spectrophotometer (Agilent Technologies; Santa Clara, California, USA) fitted with a Spectralon Nanomaterials sphere.

X-ray photoelectron spectra (XPS) were recorded using a PHI 5700 spectrometer (Physical Electronics; Chanhassen, MN, USA) with monochromatic Al Kα radiation. The binding energy shifts due to sample charging were corrected using the adventitious C 1 s peak at 284.8 eV.

An ABA-class LED solar simulator (LSH-7320, Newport Corporation; Irvine, California, USA) was used to measure the I–V curve under IEC 60904–9 standard conditions (1000 W m^{-2} irradiance, AM 1.5 G spectrum, 25 °C), connected to a VSP potentiostat (Biologic; Knoxville, Tennessee, USA).

2.6. Electrochemical measurements

The electrochemical behaviour of the electrode was analysed using a three-electrode electrochemical cell. LFO was used as the working electrode, Pt as the counter electrode, and a saturated calomel electrode (SCE) as the reference. ASC studies were conducted in a two-electrode geometry using the same VSP potentiostat (Biologic; Knoxville, Tennessee, USA).

Electrochemical measurements included cyclic voltammetry (CV), GCD, and stability tests. These measurements provided the specific capacitance (C; F g^{-1}), calculated from CV (Eq. 1) or GCD (Eq. 2), as well as energy density (E; Wh kg^{-1}), power density (P; W kg^{-1}), and coulombic efficiency (η; %), calculated from GCD using Eqs. 3, 4, and 5, respectively:

$$C = \frac{\int i(V)dV}{m \bullet v \bullet \Delta V}, \# \quad (1)$$

$$C = \frac{I \bullet \Delta t}{m \bullet \Delta V}, \# \quad (2)$$

$$E = \frac{1}{7.2} C \bullet \Delta V^2, \# \quad (3)$$

$$P = \frac{E}{\Delta t} \bullet 3600, \# \quad (4)$$

$$\eta = \frac{t_d}{t_c} \bullet 100, \# \quad (5)$$

where *i(V)* is the voltametric current (A), *m* is the mass of the active materials (g), *v* is the scan rate of the potential (V s^{-1}), *ΔV* is the potential window of the CV and of the discharge curves, *I* is the applied current (A), *Δt*and t_d are the discharge times (s), and t_c is the charging time (s).

The behaviour of the PSC was studied by monitoring the voltage evolution during photocharging under illumination, followed by galvanostatic discharge in the dark.

DSSC behaviour was assessed through I–V curves:

$$\eta_c = \frac{V_{OC} \bullet J_{sc} \bullet FF}{P_{in}}, \# \quad (6)$$

where η_c is the photovoltaic conversion efficiency (%) of the DSSC, V_{oc} is the open circuit voltage (V), J_{sc} is the short-circuit current density (mA cm^{-2}), *FF* is the fill factor (%), and P_{in} is the incident radiation power density (mW cm^{-2}).

Total irradiated energy on the DSSC (E_{DSSC}; Wh) was calculated from the illumination time (*t*; h):

$$E_{DSSC} = P_{in} \bullet t \bullet A_{DSSC}, \# \quad (7)$$

where A_{DSSC} is the illuminated area of the solar cell (cm^2) and *t* was measured as the photocharging period of the PSC.

PSC performance was evaluated by the overall efficiency (η_o), defined as the ratio between the stored energy in the PSC and E_{DSSC}:

$$\eta_{overall} = \frac{E_{st}}{E_{DSSC}}.\# \quad (8)$$

The stored energy in the PSC is denoted by E_{st}, which is the energy obtained by galvanostatic discharge under dark conditions (Wh; Eq. 3).

Finally, the storage efficiency of the PC (η_{st}) was defined as the overall efficiency corrected by the conversion efficiency of the solar cell:

$$\eta_{storage} = \frac{\eta_{overall}}{\eta_c}.\# \quad (9)$$

3. Results and discussion

3.1. Characterisation of the LFO electrode

3.1.1. Optical, morphological, structural, and chemical characterisation

Fig. 1a shows the transmission spectra of LFO thin films obtained by spray pyrolysis with deposition times of 2, 5, and 10 min on ITO/glass substrates. Transmission varies with film thickness, which increases with deposition time. Therefore, longer deposition times result in thicker films and reduced transmission in the visible (illuminant D65) and solar (AM 1.5 G) spectra, with transmission values of 0.72 (0.63), 0.54 (0.45), and 0.44 (0.36) for deposition time of 2, 5, and 10 min, respectively. Table SI-1 presents the results for the films obtained at 2, 5, and 10 min. The sheet resistivity of the LFO thin films, measured using a four-point probe, was found to increase with deposition time due to greater thickness and deposited mass, with values of 620.42 and 710.83 Ω sq^{-1} for deposition times of 2 and 5 min, respectively. A balance among visible transparency (380–770 nm), solar transparency (295–2415 nm), and electrical conductivity was achieved for LFO layers deposited for 5 min [21].

The FESEM micrographs of the electrode surface (Fig. 1b–d) depicted homogeneous LFO coating, as confirmed by the EDS elemental maps (Fig. 1e). However, the Li distribution could not be determined using EDS due to its low atomic mass.

X-ray diffraction (XRD) (Fig. 2a) revealed two peaks corresponding to cubic $LiFe_5O_8$ and the ITO substrate. The LFO peaks located at 2θ of 43.3° and 63.8° corresponded to the (400) and (440) planes, respectively (PDF 01–070–5669, International Diffraction Data Centre). Compared to reference data [23], the simplicity of the diffractogram indicated that this material contained polycrystalline cores with minute crystal sizes, resulting in broad, low-intensity signals. HRTEM analysis of an LFO lamella revealed further structural information. The fast Fourier transform (FFT) of the HRTEM cross-section image (Fig. 3) confirmed the presence of additional crystalline planes matching cubic *α* -$LiFe_5O_8$ (PDF 01–070–5669) (Fig. 2b). Additionally, the thickness of the LFO layer was determined to be 140 nm (Fig. 3d), and the absence of breaks, cracks, and discontinuities was verified. Furthermore, the distribution of Fe was found to be homogeneous (Fig. 3e).

Fig. 4 shows the XPS spectra of the Li 1 s, Fe 2p, O 1 s, and C 1 s peaks. The shift in binding energy due to sample charging was corrected using the C 1 s peak at 284.8 eV. The overlapping Fe 3p and Li 1 s peaks were fitted with two components: Fe 3p and Li 1 s [24,25]. The Fe 2p core level spectrum (Fig. 4b) showed peaks at 709.81 and 723.31 eV, which corresponded to Fe $2p_{3/2}$ (Fe^{3+}) and Fe $2p_{1/2}$ (Fe^{3+}), respectively [25], along with two shake-up satellites at 714.72 and 729.45 eV [25].

The O 1 s core level contained three peaks located at 530.0, 531.70, and 532.28 eV, which corresponded to oxygen vacancies, ordered lattice oxygen ions in the LFO, and surface hydroxyl groups from adsorbed H_2O, respectively [25]. The C 1 s core level spectrum (Fig. 4d) was fitted with three signals located at 284.73, 285.66, and 288.73 eV, which were attributed to adventitious carbon (C–C/C═C), C–O, and C═O, respectively [26]. The carbonate signal at 289.0 eV was related to the deposition technique, which was performed in an ambient atmosphere using organic precursors. A comparison of the survey spectra for pristine and cycled samples (SI Fig. 1) confirmed that the material was stable, with no significant material loss after cycling.

3.1.2. Electrochemical characterisation of the electrode

The LFO thin films were evaluated in a three-electrode cell using two aqueous solutions: 0.5 M Na_2SO_4 and 0.5 M $LiClO_4$ (Fig. 5). Figs. 5a and 5b show the CV curves for both electrolytes at scan rates ranging from 5 to 200 mV s^{-1} within a potential window of −0.7 to 0.0 V. The CV profile in the Na_2SO_4 electrolyte appeared more rectangular than that in $LiClO_4$, suggesting that surface-related capacitive-controlled processes contributed more strongly in the former. In contrast, the asymmetric CV curve in the latter indicates a predominance of semi-infinite diffusion-

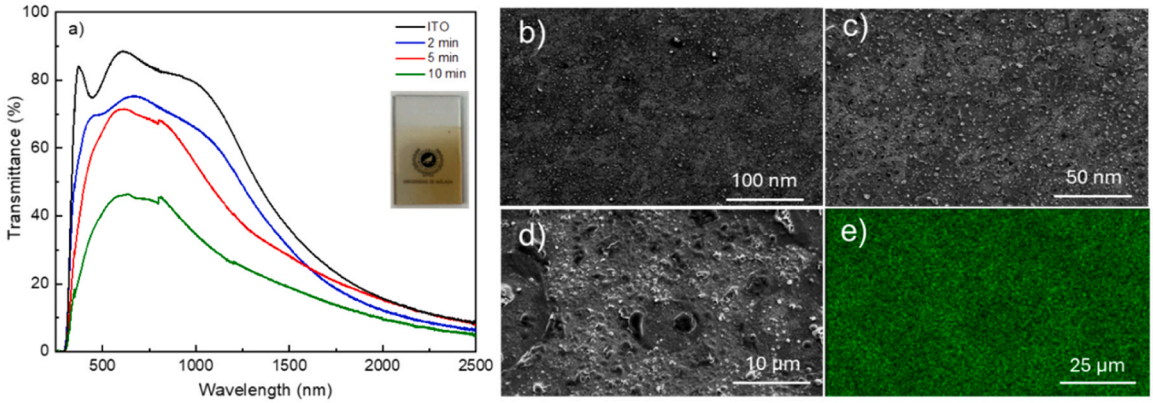

Fig. 1. Optical, morphological, and chemical properties of the LFO thin film: (a) optical transmittance spectra at different spray pyrolysis deposition times; (b–d) FESEM micrographs at different magnifications; (e) EDS elemental map for Fe.

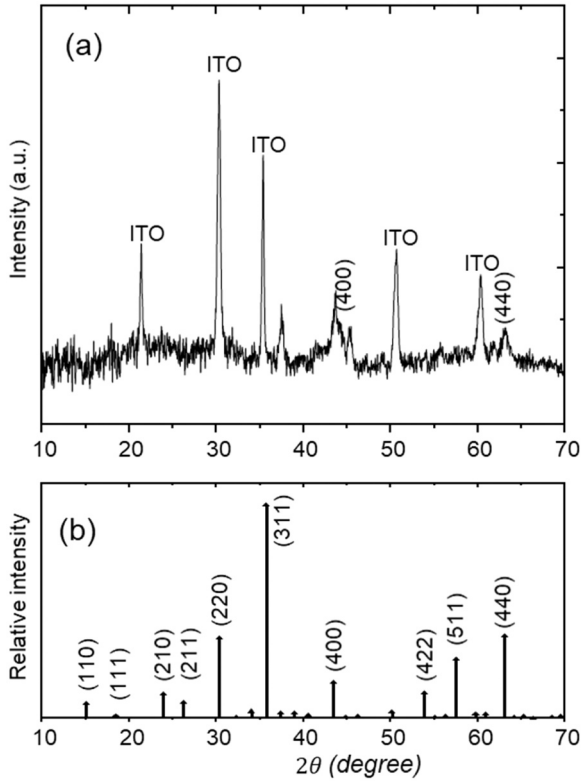

Fig. 2. XRD patterns of (a) the LFO thin film and (b) the corresponding standard reference (PDF 01–070–5669).

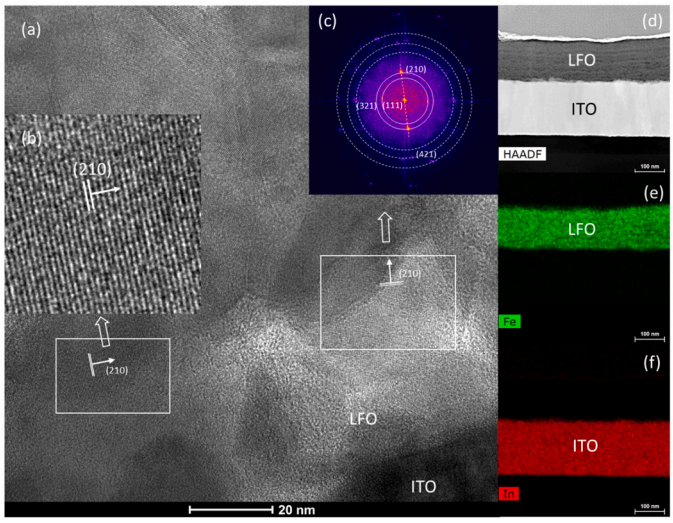

Fig. 3. LFO film characterisation: (a) XRD diffractogram. (b) HRTEM micrograph. (c–e) Identified crystalline planes and interplanar distances. (g–k) EDS elemental maps from the lamella. (h) HAADF image.

controlled processes, such as intercalation and deintercalation [27].

Both systems exhibited characteristic behaviour at scan rates above 5 mV s^{-1}, where the capacitive contribution increased with the scan rate. At high scan rates, the shorter ion diffusion time and distance between the electrolyte and active material account for this phenomenon. The highest specific capacitance was observed at a scan rate of 5 mV s^{-1}, reaching 104 and 126 F g^{-1} for Na_2SO_4 and $LiClO_4$, respectively. Additionally, the electrode maintained values of 101, 91, 88, 81, 78, 74 and 70 F g^{-1} and 104, 84, 72, 66, 62, 56 and 52 F g^{-1} at scan rates of 10, 25, 50, 75, 100, 150 and 200 mV s^{-1} for Na_2SO_4 and $LiClO_4$, respectively. These results indicate that, as the scan rate increased, the specific capacitance decreased due to the reduced time available for ions to reach the surface, where surface-controlled processes such as electric double-layer capacitance (EDLC) and pseudocapacitance occur [28–31].

The specific capacitance values measured by CV in this study were significantly higher than those reported by Lin et al. [32], who measured maximum values of 57 and 64 F g^{-1} at 5 mV s^{-1} for LFO nanoparticles and porous LFO microspheres, respectively, after 15 min of etching.

Figs. 5c and 5d show the GCD curves of the LFO electrode in Na_2SO_4 and $LiClO_4$ aqueous solutions, respectively, at specific current densities ranging from 0.5 to 3.0 A g^{-1}. At higher current densities (2.0 and 3.0 A g^{-1}), the GCD curves exhibited quasi-symmetric triangular shapes, indicating a reduced contribution from diffusion-controlled pseudocapacitive processes and, therefore, a greater involvement of the EDLC. At lower current densities (0.5 and 1.0 A g^{-1}), particularly in $LiClO_4$, the large voltage plateau matched behaviour resembling that of a battery-type electrode [27,33,34]. For instance, the first discharge at 0.5 A g^{-1} took 70 s in Na_2SO_4, compared to 38 s in $LiClO_4$, corresponding to specific capacitance values of 119 and 70 F g^{-1}, respectively, based on Eq. 2.

According to Helseth [35,36], the shape of the galvanostatic charging curve provides insight into the mechanisms contributing to specific capacitance. In Na_2SO_4 (Fig. 5c), the charging curve was concave, corresponding to type II, whereas in $LiClO_4$ (Fig. 5d) the convex shape corresponded to type I. The type II shape is attributed to a low ion concentration in the electrolyte near the surface [35,36], while the type I shape is attributed to the charge transfer of the active species on the electrode surface and is the curve most frequently observed in the

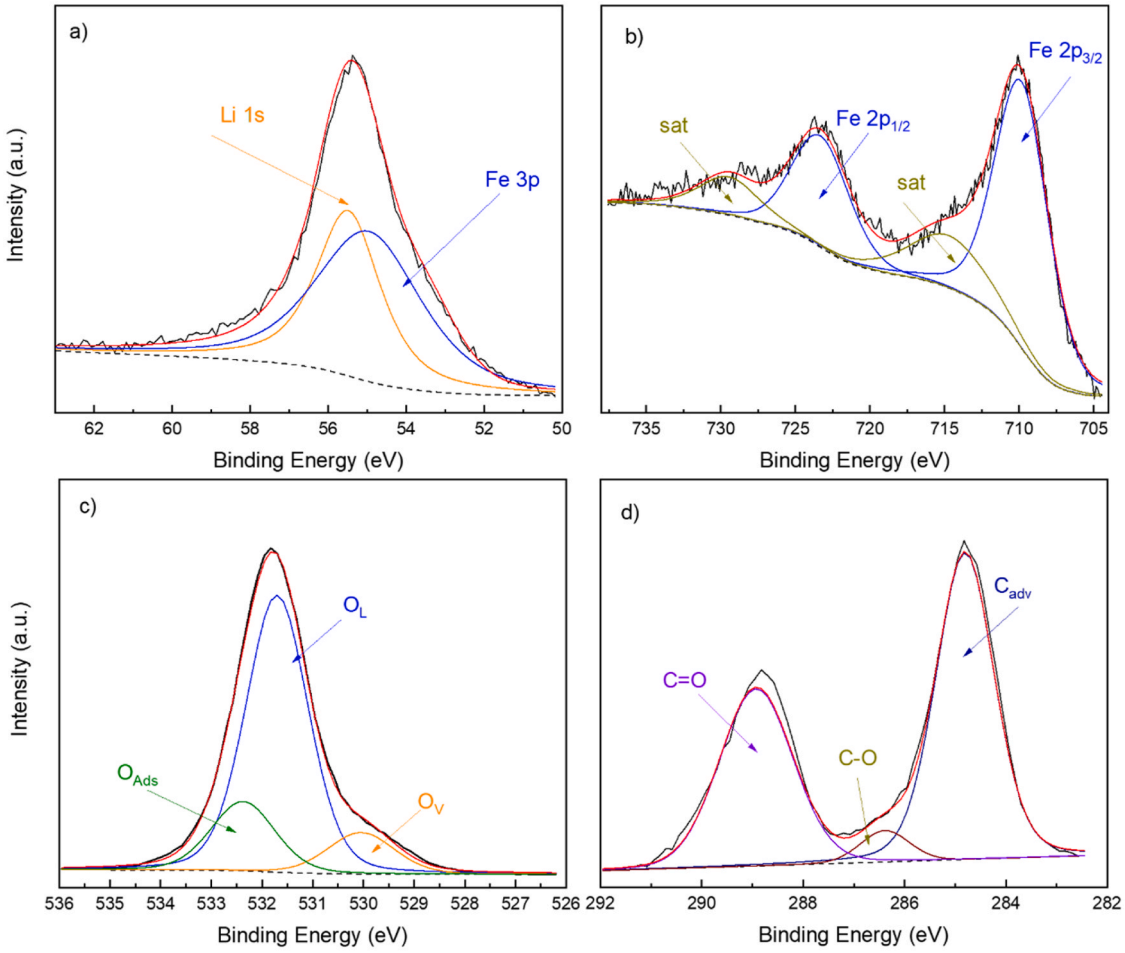

Fig. 4. XPS analysis of the LFO thin film: (a) Li 1 s, (b) Fe 2p, (c) O 1 s, and (d) C 1 s core levels.

literature.

Fig. 5e shows the evolution of specific capacitance with discharge current density. For all measurement conditions, the specific capacitance remained higher in Na_2SO_4, although $LiClO_4$ showed less dependence on discharge current density. The specific capacitance values obtained using GCD with a discharge intensity of 2 A g^{-1} were significantly higher than those reported in the literature for LFO materials with different morphologies. For example, William et al. [37] reported 0.01 F g^{-1} in LFO nanorods, whereas Lin et al. [32] obtained values of 7 and 9 F g^{-1} for nanoparticles and flower-like porous microspheres, respectively, after 15 min of etching. These values are similar in magnitude to those achieved by Dong et al. [38] for LFO nanosheets.

Fig. 5f shows Nyquist plots for the electrode in both electrolytes, with insets showing magnified views and equivalent circuits. The adopted equivalent circuit comprises the electrolyte resistance (R1), the charge transfer resistance (R2) in parallel with the double-layer capacitance (C), and a Warburg impedance, which reflects the resistance to mass transport of electrolyte species to the electrode surface when considering a semi-infinite linear diffusion [39]. Measurements taken with both electrolytes exhibited a depressed semicircle in the high/mid frequency range and a straight line at low frequencies. The R1 values were similar at 1.25 and 2 Ω cm^{-2} for Na_2SO_4 and the $LiClO_4$, respectively. However, the corresponding R2 values differed slightly at 0.63 and 12.25 Ω cm^{-2}. The larger amplitude of the semicircle for $LiClO_4$ suggests that charge transfer phenomena predominantly controlled the kinetics at high frequencies. The semicircle was minimal for Na_2SO_4, indicating dominant mass transfer processes. These results were consistent with previous discussions concerning the shapes of the CV and GCD curves.

Finally, specific capacitance retention was evaluated using continuous GCD measurements at a current density of 2 A g^{-1} (Figs. 5g and 5h). The LFO electrode exhibited superior stability with the $LiClO_4$ electrolyte, achieving 60 % capacity retention at 3000 cycles, compared to 45 % in Na_2SO_4. These findings were comparable to those obtained by Dong et al. [38], who reported a retention of 60.11 % after 3000 cycles for LFO nanosheets.

Lindström et al. [40] proposed a potential relationship between the applied scan rate, v (V s^{-1}) and the observed electrochemical current, i (A) [27,41–43]:

$$i = a \cdot v^{b}, \# \tag{10}$$

where a and b are constants that can be determined by linear regression of log i versus log v [27,41–44]. A b value of 1 indicates that the main kinetic process for energy storage is surface-controlled, such as the formation of the EDLC and surface-confined redox reactions. In contrast, a b value of 0.5 corresponds to a semi-infinite diffusion-controlled process characteristic of a battery-type redox system [27,41–43]. Values of b from 0.5 to 1.0 represent the transition between battery-type and capacitive behaviours, and therefore, the kinetic process of the electrode seems to be complex and often involves a mixed mechanism involving both diffusion and capacitive contribution or finite-length diffusion [24].

Liu et al. [45] expressed this as a combination of surface- and diffusion-controlled phenomena, relating them as follows [27,41,42]:

$$i = i_{cap} + \quad i_{diff} = k_1 v + \quad k_2 \quad v^{\frac{1}{2}}.\# \tag{11}$$

Here, i (V), $k_1 v$, and $k_2 v^{1/2}$ represent the total current at fixed

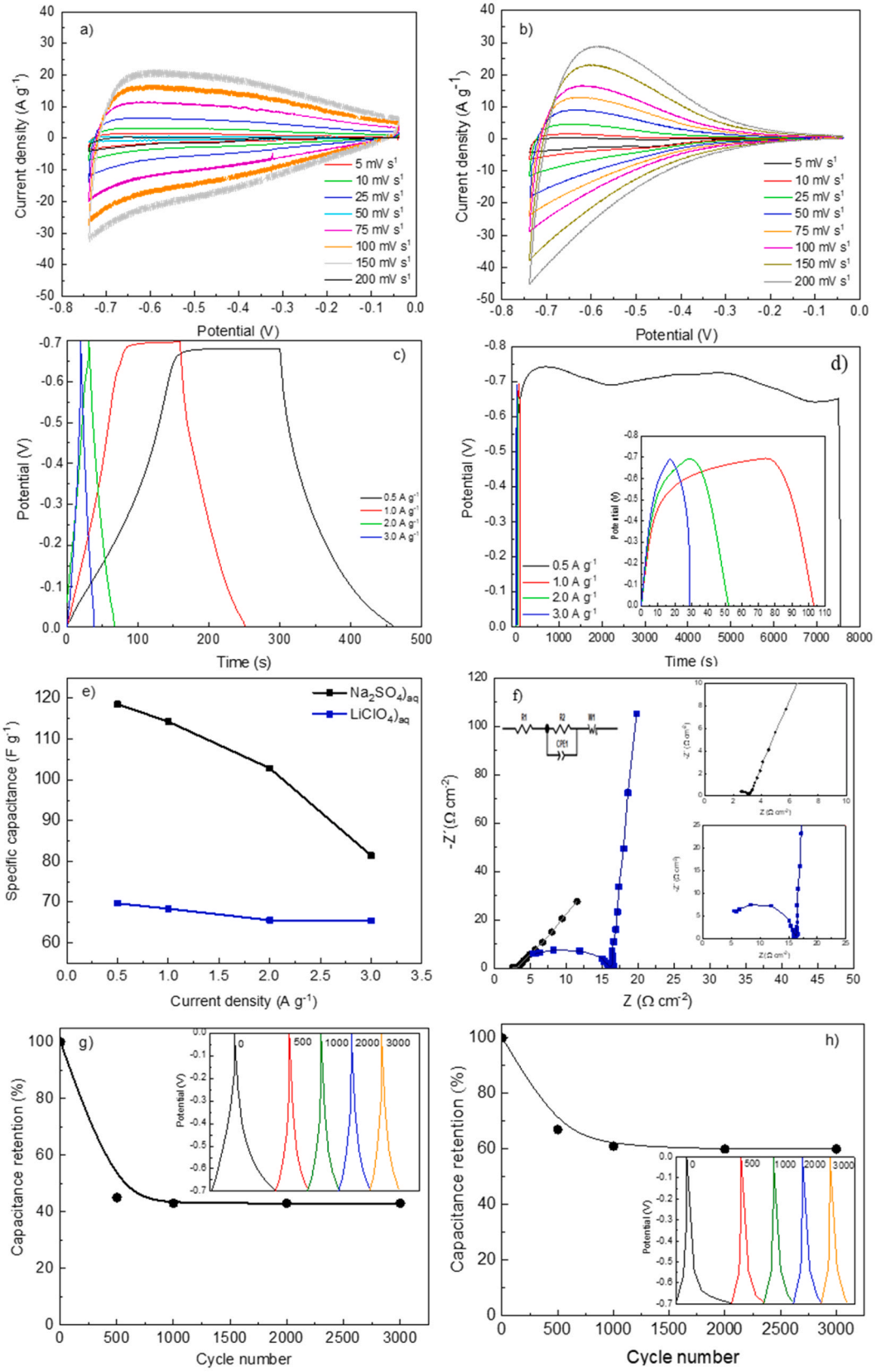

Fig. 5. Electrochemical characterisation of the LFO electrode cycled in different aqueous electrolytes, Na_2SO_4 (left) and $LiClO_4$ (right): (a, b) CV at varying scan rates. (c, d) GCD at varying current densities. (e) Specific capacitance evolution for both electrolytes. (f) Impedance spectroscopy analysis results for both electrolytes. (g, h) Cycling stability test results.

potentials, the current from the pseudocapacitance contribution, and the current from the diffusion contribution, respectively. These can be expressed linearly as follows [27,46]:

$$\frac{i}{v^{\frac{1}{2}}} = k_1 \quad v^{\frac{1}{2}} + \quad k_2.\# \tag{12}$$

The k_1 and k_2 values are the obtained slope and intercept, respectively. According to Ardizzone et al. [47], the specific capacitance (Q) of the electrode, expressed per unit mass of the active material, can be expressed as follows [27,43]:

$$Q = \quad Q_\infty + constant v^{\frac{-1}{2}}, \# \tag{13}$$

where extrapolating the fitted line to $v^{-1/2} \rightarrow 0$ (infinite scan rate) yields $Q\infty$, which reflects the electrostatic (adsorption) contribution near the surface due to fast processes. These processes are always active, even at high scan rates, whereas the capacitance contribution from semi-infinite linear diffusion processes varies with $v^{-1/2}$.

The results obtained are shown in Fig. 6. The calculated *b*-values (Eq. 10) differed significantly depending on the electrolyte: approximately 1.0 for Na_2SO_4 (Fig. 6a) and 0.5 for $LiClO_4$ (Fig. 6b), indicating distinct charge storage mechanisms and kinetics. For Na_2SO_4, faster ion diffusion-independent mechanisms were dominant, including the electrical double layer formation and fast faradaic reactions involving surface-located redox species. In contrast, $LiClO_4$ exhibited a predominance of slower ionic diffusion-dependent mechanisms involving the entire electrode material, such as ionic intercalation and deintercalation.

However, these behaviours vary with scan rate, as shown in Figs. 6c and 6d and explained by Eq. 13. At low scan rates during electrode cycling in $LiClO_4$, diffusion-dependent charge storage kinetics predominate. This was favoured by the presence of Li^+ (66 % versus 34 % for diffusion-dependent and diffusion-independent kinetics, respectively, at 5 mV s^{-1}). However, the current related to diffusion processes decreased with increasing scan rate, highlighting the limited time available for electrolyte ions to diffuse into the electrode (17 % versus 83 % for diffusion-controlled and diffusion-independent processes, respectively). For all scan rates, the charge storage kinetics of the electrode cycled in Na_2SO_4 were mainly driven by fast processes such as the electrochemical double layer formation and surface phenomena (66 % versus 34 % for diffusion-dependent and diffusion-independent kinetics, respectively, at 5 mV s^{-1}). At high scan rates, these processes nearly completely dominated. Finally, the extrapolated $Q\infty$ values were 67.23 and 43.25 F g^{-1} for Na_2SO_4 and $LiClO_4$, respectively, reflecting the lower response of $LiClO_4$ to diffusion-independent processes.

3.2. SC electrochemical performance

The electrochemical characterisation of the ASCs in the form of two assembled electrodes, one with El-Na_2SO_4 and the other with El-PVP-$LiClO_4$, is shown in Fig. 7. Figs. 7a and 7b show the CV curves for both devices, which were performed at scan rates from 5 to 200 mV s^{-1} and within a potential range of 0.0–1.9 V. For the ASC assembled with the El-Na_2SO_4 aqueous electrolyte (Fig. 7a), a Faradaic contribution was observed at 0.83 V due to the non-symmetric redox process associated with the extraction of Zn^{2+} from the $ZnMn_2O_4$ spinel, as previously reported by our group [21]. These Faradaic reactions are undesirable, as they lead to electrode corrosion. Additionally, the negligible variation in

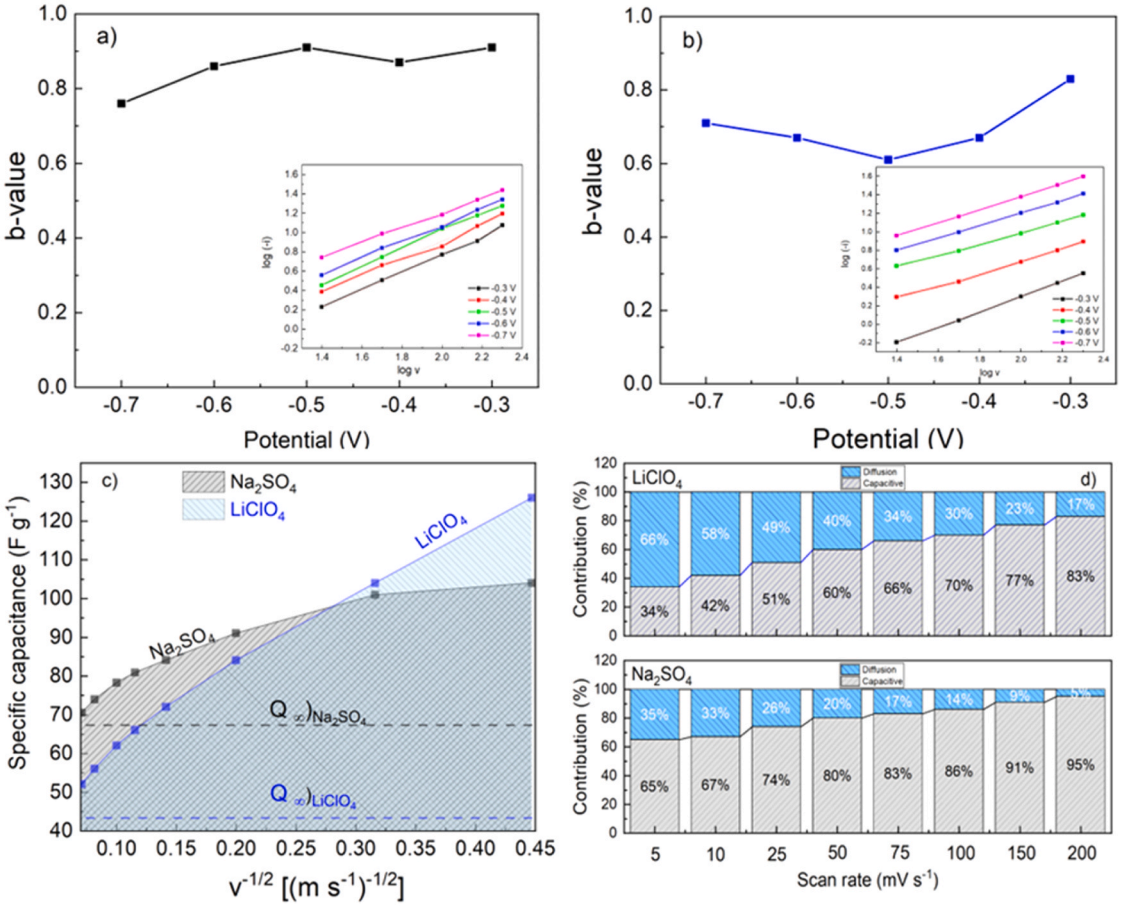

Fig. 6. Electrode behaviour based on electrolyte type: *b*-values determined for (a) Na_2SO_4 and (b) $LiClO_4$. (c) Relationship between specific capacitance and scan rates. (d) Contribution of independent and dependent diffusion-driven processes for Na_2SO_4 and $LiClO_4$ electrolytes.

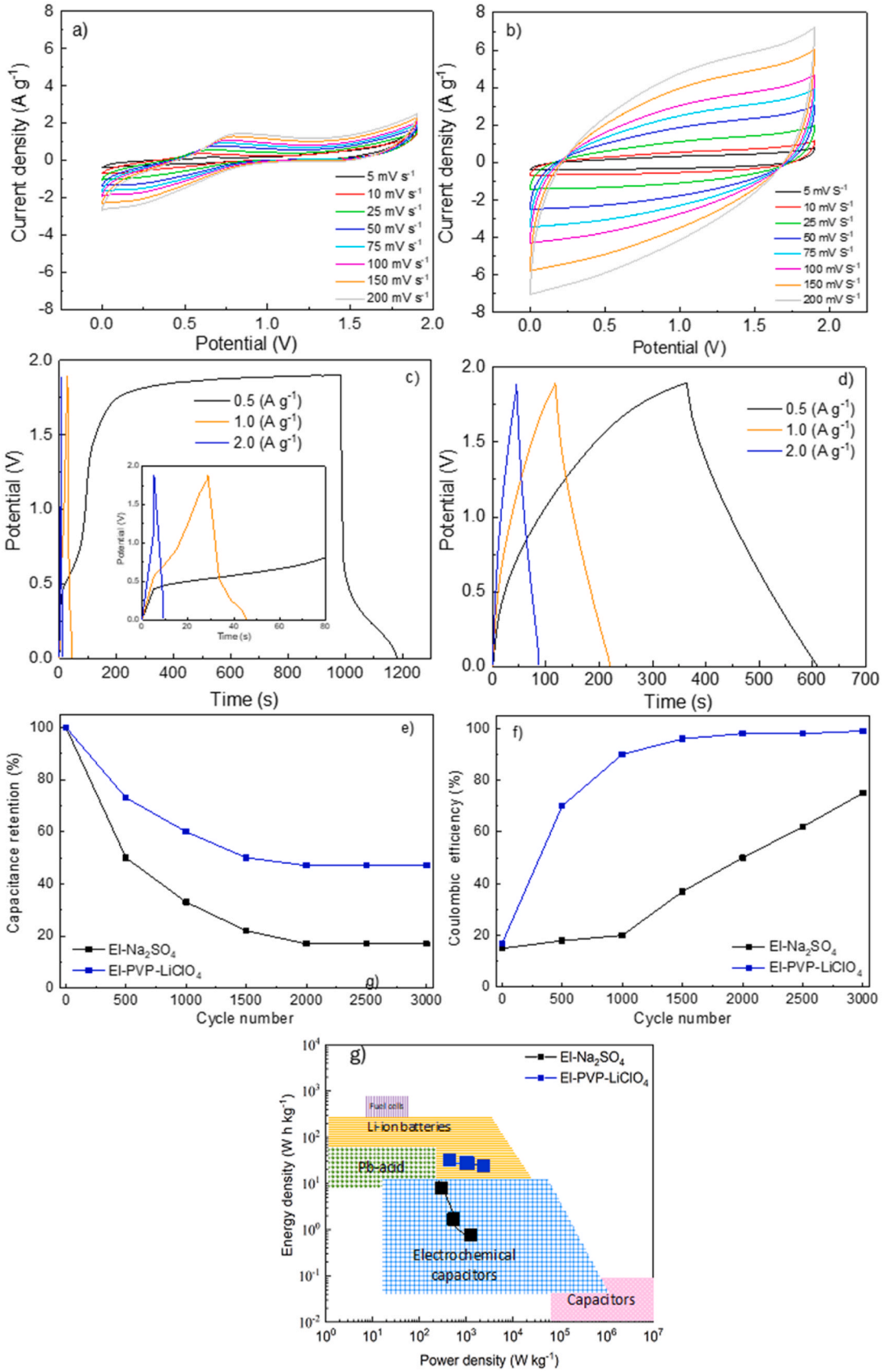

Fig. 7. ASC analysis for El-Na_2SO_4 (left) and El-PVP-$LiClO_4$ (right) electrolytes: (a, b) CV at different scan rates. (c, d) GCD. (e) Capacitance retention and (f) coulombic efficiency for El-Na_2SO_4 (black) and El-PVP-$LiClO_4$ (blue). (g) Ragone plot and position of the two ASCs assembled with El-Na_2SO_4 (black) and El-PVP-$LiClO_4$ (blue).

CV curve area with scan rate indicates that charge accumulation and release mainly occurred via capacitive processes at the electrode–electrolyte interface, driven by electrostatic interactions [43]. In contrast, the ASC assembled with El-PVP-$LiClO_4$ (Fig. 7b) avoided corrosion, resulting in voltammograms that deviated from the typical rectangular shape of EDLCs. These curves are associated with diffusive processes, leading to higher current responses and enhanced ASC performance [48–51].

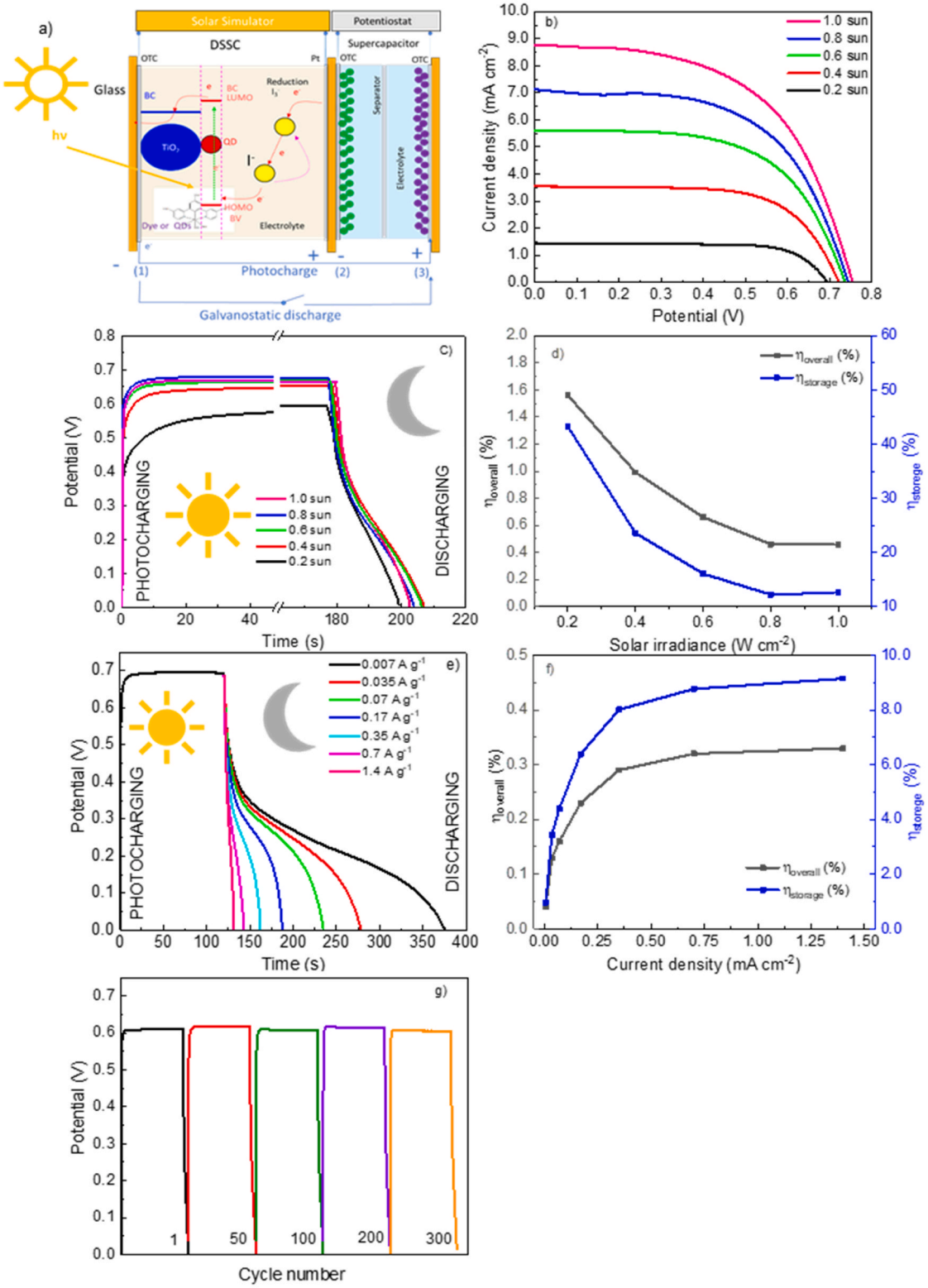

Fig. 8. Performance characterisation of the DSSC/ZMO/El-PVP-$LiClO_4$/LFO integrated PSC: (a) Schematic of the PSC with wiring diagram. (b) I–V curve of the DSSC measured at different irradiance levels. (c) PSC performance at different irradiance levels under a constant discharge current density of 12.5 μA cm^{-2}. (d) Evolution of $\eta_{storage}$ and $\eta_{storage}$ with irradiance level. (e) PSC performance under 1.0 sun and various discharge current densities. (f) Evolution of $\eta_{storage}$ and $\eta_{storage}$ with discharge current density. (g) Stability test over 300 photocharging and discharging cycles.

The highest specific capacitance values were 26 and 54 F g^{-1} at 5 mV s^{-1} for El-Na_2SO_4 and El-PVP-$LiClO_4$, respectively. Additional values were 19, 11, 7, 6, 5, 4, and 3 F g^{-1} and 46, 37, 30, 27, 24, 21, and 18 F g^{-1} at scan rates of 10, 25, 50, 75, 100, 150, and 200 mV s^{-1} for El-Na_2SO_4 and El-PVP-$LiClO_4$, respectively.

Figs. 7c and 7d show the GCD curves for the two ASCs at current densities of 0.5, 1.0, and 2.0 A g^{-1}. In the El-Na_2SO_4 device, a rapid increase in potential was recorded during the initial stage of charging, reflecting the rapid formation of the electrochemical double layer. The charging times varied significantly with current density, reaching 983, 29, and 5 s for 0.5, 1.0, and 2.0 A g^{-1}, respectively [43]. Furthermore, the plateau zone in the charge curve was attributed to irreversible Zn loss in the $ZnMn_2O_4$ anode [21]. The discharge process also exhibited a significant potential drop due to the presence of internal series resistance. In contrast, the GCD curves for the El-PVP-$LiClO_4$ device (Fig. 7d) exhibited a nearly triangular shape, indicating the presence of diffusion-controlled processes. Charging times were 364, 118, and 45 s for current densities of 0.5, 1.0, and 2.0 A g^{-1}, respectively, followed by a sustained discharge [43]. These two behaviours resulted in different specific capacitances of 52, 9, and 4 F g^{-1} and 64, 54, and 44 F g^{-1} for El-Na_2SO_4 and El-PVP-$LiClO_4$, respectively, at current densities of 0.5, 1.0, and 2.0 A g^{-1}.

The long-term stability of both ASCs was assessed using GCD at 2 A g^{-1} (Fig. 7e). After an initial decrease, both ASCs demonstrated high stability for the duration of the test, retaining 20 % and 50 % of their initial capacitance after 3000 cycles for El-Na_2SO_4 and El-PVP-$LiClO_4$, respectively.

The coulombic efficiency analysis is presented in Fig. 7f. The symmetry between the charge and discharge processes resulted in values exceeding 80 % (after stabilisation of the ASC) for the device assembled with El-PVP-$LiClO_4$, whereas the device assembled with El-Na_2SO_4 exhibited lower values. The energy and power densities of both devices were calculated and plotted in the Ragone diagram (Fig. 7g). The corresponding energy densities were 13, 2, and 1 Wh kg^{-1} and 32, 27, and 22 Wh kg^{-1}, and the power densities were 237, 475, and, 950 W kg^{-1} and 473, 950, and 1900 kg^{-1} based on discharge current densities of 0.5, 1.0, and 2.0 A g^{-1} for devices assembled with El-Na_2SO_4 and El-PVP-$LiClO_4$, respectively. These results, as shown in the Ragone diagram, clearly demonstrate the influence of electrolyte composition on the characteristics of the device, defining it as either a typical electrochemical SC or a nearly hybrid SC.

3.3. PSC electrochemical performance

Fig. 8a shows a diagram of the characterised three-electrode PSC, comprising the assembled DSSC-type solar cell (TiO_2/N719/I^--I_3^-/Pt) and the ASC (ZMO/El-PVP-$LiClO_4$/LFO). Evaluation of the PSC required individual characterisation of each unit (DSSC in this section and SC in Section 3.2), and of the integrated self-charging ASC. The solar cell was assessed by varying the irradiance from 1000 (1.0 sun) to 200 W m^{-2} (0.2 sun) and measuring the I–V curves at a constant temperature of 25 ºC. The working PSC was photocharged by illuminating the device with the solar simulator, which automatically connected electrodes 1 and 3 (Fig. 8a). During the discharge process, the solar simulator was switched off, and electrodes 1 and 3 were automatically disconnected.

Fig. 8b shows the typical response of a solar cell. The J_{sc} decreased significantly with irradiance, from 8.779 to 1.426 mA cm^{-2} at 1.0 and 0.2 sun, respectively, while the V_{oc} only responded significantly at lower irradiances, varying from 0.754 to 0.693 V at 1.0 and 0.2 sun, respectively. Consequently, the power generated by the cell decreased from 0.913 to 0.036 W for 1.0 and 0.2 sun, respectively (Table SI-4).

The photoelectrochemical performance of the PSC was evaluated using GCD measurements. Fig. 8c shows the PSC response to varying irradiance levels during the photocharging process, with a constant discharge current density. This measurement is directly related to that shown in Fig. 8b. The figure indicates that the variation in irradiance level during photocharging has a greater effect at lower levels. For irradiance levels between 1.0 and 0.4 sun, the potential stabilised within the first 10 s, varying within a small range of 0.680–0.647 V. In contrast, at 0.2 sun, stabilisation took longer, with the potential falling to 0.600 V. The same current density of 12.5 μA cm^{-2} was applied throughout the discharge phase of each test. The discharge curves exhibited a similar trend, with a significant initial potential drop due to series resistance losses, followed by rapid discharge. Discharge times decreased from 33 to 22 s for photocharging at 1.0 and 0.2 sun, respectively. This enabled the calculation of real capacitances per unit area of 1.2 and 0.8 mF cm^{-2} for 1.0 and 0.2 sun, respectively, and the corresponding energy densities of 2.28 and 1.55 mWh kg^{-1}.

The performance of the PSC was evaluated by calculating two ratios. The first, storage efficiency ($\eta_{storage}$), relates the energy stored to the energy converted by the solar cell (Eq. 9), while the second, overall efficiency ($\eta_{overall}$), relates the energy stored to the total incident energy from the solar simulator (Eq. 8).

As shown in Fig. 8d, when the irradiance decreases from 1 to 0.2 sun, the $\eta_{storage}$ increases from 12.59 % to 43.20 % (blue line) and $\eta_{overall}$ from 0.46 % to 1.46 % (black line). In other words, despite a minimal power output of the solar cell at 0.2 sun, nearly half of the energy was stored in the SC, although the system became less efficient as irradiance increased. This behaviour highlights the suitability of the PSC for indoor use. Similar trends have been reported for DSSCs and thin-film SCs. In particular, Scalia et al. [52,53] reported a similar $\eta_{overall}$ of 1.46 %, but a significantly lower $\eta_{storage}$ of 3.72 % at 0.3 sun [54].

A second set of tests was conducted under 1 sun, where the discharge current density was varied from 7 mA g^{-1} to 1.4 A g^{-1} (Fig. 8e). The graph indicates that the maximum potential was attained after approximately 10 s, with varying discharge curves depending on the current density. The PSC discharged up to 0.580 V; then, as the current density increased, the discharge time reduced without altering the shape of the curve. A plateau was observed at lower discharge current densities (7.00–0.17 mA g^{-1}), indicating diffusion-controlled processes such as Li^+ intercalation. This behaviour resembled that of a battery. At higher current densities (0.37–1.40 mA g^{-1}), the device discharged rapidly due to surface-controlled processes associated with the EDLC, as shown by the linear discharge curve. Discharge times ranged from 255 to 12 s, corresponding to stored capacitance ranging from 0.09 to 0.86 mF cm^{-2} and energy densities from 0.18 to 1.66 mWh kg^{-1}.

The efficiency parameters are shown in Fig. 8f, where $\eta_{storage}$ decreases from 9.15 % to 0.97 % (blue line) and $\eta_{overall}$ from 0.33 % to 0.04 % for current densities of 7 mA g^{-1} to 1.4 A g^{-1} (black line). This indicates that device performance improved at higher current densities. These findings were consistent with previously reported values for three-electrode PSC systems combining DSSC-based photogeneration and thin-film SC storage [55] (Table SI-3).

Finally, the device stability was assessed over 300 photocharging and discharging cycles under 1.0 sun and 0.7 A g^{-1}. The results indicate that the potential remained stable over time (Fig. 8g). Notably, the device retained 81 % of its initial $\eta_{overall}$ after 300 cycles, which was a significant achievement.

4. Conclusions

In summary, α-$LiFe5O_8$ thin film electrodes were successfully prepared by spray pyrolysis and assembled into both an ASC and a three-electrode PSC. Electrochemical studies of the electrodes demonstrated their duality based on the electrolyte used, with a predominance of surface-controlled processes in Na_2SO_4 and diffusion-controlled processes in $LiClO_4$. Similarly, this difference was reflected in the two ASCs prepared with a ZMO anode. With the aqueous Na_2SO_4 electrolyte, the ASC exhibited inferior performance, and the anode underwent significant corrosion-related degradation. In contrast, the semi-solid PVP-based electrolyte containing $LiClO_4$ resulted in battery-like behaviour, achieving the highest specific capacitance (64 F g^{-1}), energy density

(32 Wh kg^{-1}) and power density (473 W kg^{-1}), with 50 % capacity retention after 3000 cycles.

Finally, the PSC prepared by coupling a dye cell demonstrated that the photocharging process was largely independent of the irradiance level. This would enable device operation under indoor lighting and allow the system to behave as either a battery or electrochemical SC, depending on the applied discharge current densities. The best performance was achieved at a solar irradiance of 0.2 sun and a discharge current of 12.5 μA cm^{-2}, resulting in storage and overall efficiencies of 43.20 % and 1.46 %, respectively.

CRediT authorship contribution statement

Dr. Francisco Martín Jiménez: Writing – original draft, Funding acquisition, Formal analysis. **Juan José Peinado Pérez:** Investigation, Data curation. **M.C. López-Escalante:** Writing – review & editing, Writing – original draft, Supervision, Methodology, Investigation, Formal analysis, Data curation, Conceptualization.

Declaration of Competing Interest

The authors declare that they have no conflicts of interest.

Acknowledgements

The authors are grateful for the support received by the Spanish Ministry of Science and Innovation through the research project PID2020–117832RB-100 and the Junta de Andalucía, Feder Funds through project FQM192-G-FEDER 2023–2025.

Appendix A. Supporting information

Supplementary data associated with this article can be found in the online version at doi:10.1016/j.jallcom.2025.182400.

References

[1] N. Sangiorgi, A. Sangiorgi, A. Soccio, M. Rancan, L. Armelao, A. Sanson, Bifunctional WO_3 photoelectrodes decorated by inkjet printing for solar supercapacitors, Adv. Sustain. Syst. (2025) e00478, https://doi.org/10.1002/adsu.202500478.

[2] P. Joselene Suzan, S. Muthupandi, A. Angelin, M. Joe Raja Ruban, D. Annie Canisius, D. Varghese, M. Gladys, J. Madhavan, M.V.A. Raj, Integrating Pt-free dye-sensitized solar cell and symmetric supercapacitor employing common electrode quaternary nanocomposite, NanoStruct. NanoObjects 40 (2024) 101411, https://doi.org/10.1016/J.NANOSO.2024.101411.

[3] N. Flores-Diaz, F. De Rossi, T. Keller, H. Morritt, Z. Perez Bassart, A. Lopez-Rubio, M. Jose Fabra, R. Freitag, A. Gagliardi, F. Fasulo, A.B. Muñoz-García, M. Pavone, H. Javanbakht Lomeri, S. Sanchez Alonso, M. Grätzel, F. Brunetti, M. Freitag, Unlocking high-performance photocapacitors for edge computing in low-light environments, Energy Environ. Sci. 18 (2025) 4704–4716, https://doi.org/10.1039/D5EE01052G.

[4] A. Bibi, M. Mustaqeem, M.A. Gondal, A. Majeed, P.T. Chou, Y.F. Chen, Z.G. Gu, M. Waqas, A. Ali, Recent progress and challenges in photo-supercapacitors: a critical review along with future prospects, J. Energy Storage 123 (2025) 116696, https://doi.org/10.1016/J.EST.2025.116696.

[5] V.K. Sriramadasu, N. Jayababu, S. Bhattacharyya, Red carbon dots sensitized Ni-doped 2D MoS_2 nanosheets as electrode materials for visible-light active photorechargeable supercapacitors, Small Struct. 6 (2025) 2400480, https://doi.org/10.1002/sstr.202400480.

[6] Z. Hosseini, M.M. Momeni, B.K. Lee, A.W. Maijenburg, Light-Enhanced capacitive performance in $LaFeO_3$-based photo-supercapacitors employing p-n heterojunction architecture, Chem. Eng. J. 515 (2025) 163566, https://doi.org/10.1016/J.CEJ.2025.163566.

[7] C.S. Rout, P. Shinde, M.A. Belgami, J.S. Cho, S.M. Jeong, Halide perovskites for supercapacitors and photosupercapacitors: recent developments and future perspectives, Small (2025) e2503138, https://doi.org/10.1002/smll.202503138.

[8] P.S. Chauhan, M. Parekh, S. Sahoo, S. Kumar, A.Das Mahapatra, P. Sharma, V. Panwar, A.M. Rao, A. Misra, Influence of electrolyte on the photo-charging capability of a ZnO-FTO supercapacitor, J. Mater. Chem. A 12 (2024) 22725–22736, https://doi.org/10.1039/d4ta04702h.

[9] I. Naskar, A.K. Ray, M. Freitag, M. Deepa, Zn/Mg metal-organic framework composite for energy storage via cobalt phthalocyanine dye in a self-powered photosupercapacitor, Electrochim. Acta 513 (2025) 145526, https://doi.org/10.1016/J.ELECTACTA.2024.145526.

[10] S. Persson, I. Benesperi, Y. Goriya, D. Kand, S. Rayavarapu, T. Keller, M. Freitag, K. Wärnmark, Push–pull amino-substituted heteroleptic iron N-heterocyclic carbene photosensitizers in dye-sensitized solar cells: optimization and characteristics, Sustain. Energy Fuels 9 (2025) 2389–2395, https://doi.org/10.1039/D4SE01772B.

[11] A.K. Ray, D. Maity, B. Kaur, I. Naskar, M. Deepa, Polyoxometalates PMo_{12} and $\{Mo_{132}\}$ control energy conversion and storage in an integrated perovskite solar cell-supercapacitor assembly, J. Energy Storage 109 (2025) 115145, https://doi.org/10.1016/J.EST.2024.115145.

[12] S. Khazraei, J. Palosaari, J. Peräntie, A. Selent, M. Freitag, J. Hannu, Synergistic enhancement of DSSC performance via Ti_3C_2 MXene-modified copper redox electrolytes: mechanistic insights into charge transfer and recombination, J. Power Sources 642 (2025) 237019, https://doi.org/10.1016/j.jpowsour.2025.237019.

[13] S.K. Bhaumik, S. Biswas, N. Shauloff, A. Morag, R. Jelinek, Photo-rechargeable organic supercapacitor via light-activated electrolytes, Adv. Sci. (2025) 2500978, https://doi.org/10.1002/advs.202500978.

[14] N. Sivakumar, P. Nagaraju, A. Alsalme, A. Alghamdi, R. Jayavel, Enhanced electrochemical performance of lanthanum ferrite decorated reduced graphene oxide nanocomposite electrodes prepared by in situ microwave irradiation for energy storage applications, Int. J. Energy Res. 45 (2021) 5272–5282, https://doi.org/10.1002/er.6146.

[15] K. Sedumathavan, N. Sivakumar, A. Alsulmi, K.Y. Kumar, K. Settu, A comprehensive exploration of pure and Zn doped $LaFeO_3$ nanoparticles synthesized by solid state mechanism for charge storage devices, J. Mater. Sci. Mater. Electron 35 (2024) 1791, https://doi.org/10.1007/s10854-024-13483-7.

[16] N. Sivakumar, J. Gajendiran, A. Alsalme, K. Tashiro, Structural, morphological, optical, magnetic and electrochemical behavior of solid state synthesized pure and Sr-doped $LaFeO_3$ nanoparticles, Phys. B Condens. Matter 641 (2022) 414086, https://doi.org/10.1016/J.PHYSB.2022.414086.

[17] Y. Xu, A. Liu, Y. He, K. Yang, Z. Tang, B. Zhang, Enhanced pseudocapacitance of amino-functionalized graphene films for supercapacitors across a wide pH range, J. Alloy. Compd. 1035 (2025) 181363, https://doi.org/10.1016/J.JALLCOM.2025.181363.

[18] M.M. Momeni, H.M. Aydisheh, B.-K. Lee, A. Naderi, Lightweight flexible self-powered photo-supercapacitors with good stability through photoelectrochemical deposition of tellurium on PPy–V_2O_5 films as a new visible light active dual photoelectrode, J. Mater. Chem. C. Mater. 13 (2025) 430–444, https://doi.org/10.1039/D4TC03090G.

[19] M.S. Akhter, B. Moossa, R. Kahraman, S. Rasul, R.A. Shakoor, Advancements in high voltage, high-energy density, lithium-ion cathode materials: a focused review, Appl. Mater. Today 45 (2025) 102827, https://doi.org/10.1016/J.APMT.2025.102827.

[20] A.A. Zabolotnyi, A.V. Motseyko, S.P. Kubrin, A.S. Komlev, S.A. Guda, Y.V. Rusalev, A.V. Nazarenko, N.V. Ter-Oganessian, Synthesis, magnetic and structural properties of (1-x)$LiFe_5O_8$–(x)$LiZn_{2.5}Ti_{2.5}O_8$ spinel solid solutions, J. Alloy. Compd. 1010 (2025) 177205, https://doi.org/10.1016/J.JALLCOM.2024.177205.

[21] J.J. Peinado-Pérez, M.C. López-Escalante, F. Martín, Effect of the nature of the electrolyte on the behavior of supercapacitors based on transparent $ZnMn_2O_4$ thin films, Nanomaterials 13 (2023) 3017, https://doi.org/10.3390/nano13233017.

[22] Y. Yıldız, K. Bilen, A. Atılgan, Developing hybrid TiO_2–multiwalled carbon nanotubes photoanodes for dye-sensitized solar cells, Energy Technol. (2025) 2401946, https://doi.org/10.1002/ente.202401946.

[23] J. Li, L. He, C. Du, W. Xia, D. Zhou, Honeycomb $LiFe_5O_8$/PANI nanocomposites with enhanced microwave absorption performance, Ceram. Int. 51 (2025) 7252–7262, https://doi.org/10.1016/j.ceramint.2024.12.160.

[24] H. Wang, S. Alamri, S. Formanova, Y. Wang, Structural, optical and reflection loss features of biomass-derived 2D porous carbon nanosheets in ultrathin bilayer configuration integrated with g-C_3N_4/$LiFe_5O_8$ nanocomposite for stealth applications of drone (In press,), Ceram. Int. (2025), https://doi.org/10.1016/j.ceramint.2025.05.432.

[25] Renu, T. Garg, J. Kaur, S. Bansal, A. Kaushik, S. Singhal, Fabrication of novel Ag_3PO_4/$LiFe_5O_8$ nanocomposites for dual applications in sustainable photocatalytic removal of harmful antibiotics and ratiometric electrochemical detection of hazardous carbendazim insecticide, Sustain. Mater. Technol. 39 (2024) e00800, https://doi.org/10.1016/j.susmat.2023.e00800.

[26] J.J.P. Pérez, D. Solís-Cortés, F.M. Jiménez, M.C.L. Escalante, Reduced band gap $SrTiO_3$ thin film prepared by magnetron sputtering for the oxygen evolution reaction, Mater. Today Commun. 41 (2024) 110492, https://doi.org/10.1016/J.MTCOMM.2024.110492.

[27] N. Singh, V. Singh, N. Bisht, P. Negi, A. Dhyani, R.K. Sharma, B.S. Tewari, A comprehensive review on supercapacitors: basics to recent advancements, J. Energy Storage 121 (2025) 116498, https://doi.org/10.1016/J.EST.2025.116498.

[28] A. Murugan, V. Siva, A.Samad Shameem, S.A. Bahadur, Effect of Zn on nanoscale quaternary Cu_2ZnSnS_4 thin film electrodes for high performance supercapacitors, J. Energy Storage 44 (2021) 103423, https://doi.org/10.1016/j.est.2021.103423.

[29] A. Murugan, V. Siva, A.Samad Shameem, S.A. Bahadur, Optimization of adsorption and reaction time of SILAR deposited Cu_2ZnSnS_4 thin films: structural, optical and electrochemical performance, J. Alloy. Compd. 856 (2021) 158055, https://doi.org/10.1016/j.jallcom.2020.158055.

[30] A. Murugan, V. Siva, A.S. Shameem, S.A. Bahadur, Improved electrochemical performance of nanostructured binder free $Cu_2CoSnS4$ electrode using redox additive electrolyte, Inorg. Chem. Commun. 156 (2023) 111119, https://doi.org/10.1016/j.inoche.2023.111119.

[31] A. Surulinathan, H. Gubendran, B. Sambandam, S. Ganapathy, A. Ayyaswamy, Mixed metal oxide-based binder-free electrode and redox additive electrolyte

combination for enhanced supercapacitor performance, J. Alloy. Compd. 988 (2024) 174164, https://doi.org/10.1016/J.JALLCOM.2024.174164.
[32] Y. Lin, J. Dong, J. Dai, J. Wang, H. Yang, H. Zong, Facile synthesis of flowerlike $LiFe_5O_8$ microspheres for electrochemical supercapacitors, Inorg. Chem. 56 (2017) 14960–14967, https://doi.org/10.1021/acs.inorgchem.7b02257.
[33] S.A. Thomas, J. Cherusseri, M.R. Pallavolu, M. Afzal, D.N. Rajendran, Strategically-designed environment-friendly tin-based electrodes for sustainable supercapatteries with high specific capacity, Electrochim. Acta 522 (2025) 145846, https://doi.org/10.1016/J.ELECTACTA.2025.145846.
[34] N.K. Sakthivel, M. Govindasamy, P.-Y. Chen, Sonochemical synthesis of perovskite embedded with carbon nanofibers as an electrode material for energy storage application, J. Electrochem. Soc. 172 (2025) 040519, https://doi.org/10.1149/1945-7111/adc952.
[35] L.E. Helseth, The nonlinearities in the galvanostatic charging curves of supercapacitors provide insights into charging mechanisms, J. Energy Storage 55 (2022) 105440, https://doi.org/10.1016/j.est.2022.105440.
[36] M. Shafiei, M.M. Momeni, H.M. Aydisheh, Porous manganese-nickel-cobalt oxide nanosheets electrodeposited on nickel foam as an electrode for the fabrication of flexible asymmetric hybrid supercapacitors (In press,), Ceram. Int. (2025), https://doi.org/10.1016/J.CERAMINT.2025.06.150.
[37] J.J. William, I.M. Babu, G. Muralidharan, Lithium ferrite (α-$LiFe_5O_8$) nanorod based battery-type asymmetric supercapacitor with NiO nanoflakes as the counter electrode, N. J. Chem. 43 (2019) 15375–15388, https://doi.org/10.1039/C9NJ03774H.
[38] J. Dong, Y. Lin, H. Zong, H. Yang, Hierarchical $LiFe_5O_8$ @PPy core-shell nanocomposites as electrode materials for supercapacitors, Appl. Surf. Sci. 470 (2019) 1043–1052, https://doi.org/10.1016/j.apsusc.2018.11.204.
[39] L. Li, J. Huo, Q. Ran, X. Liu, Three-dimensional carbon nanotube framework enables low-cost $LiFe_5O_8$ anode material for high-performance lithium-ion batteries, Surf. Interface Anal. 56 (2024) 799–807, https://doi.org/10.1002/sia.7347.
[40] H. Lindström, S. Södergren, A. Solbrand, H. Rensmo, J. Hjelm, A. Hagfeldt, S. E. Lindquist, Li^+ ion insertion in TiO_2 (Anatase), voltammetry on nanoporous films, J. Phys. Chem. 101 (1997) 7717–7722. ⟨https://pubs.acs.org/sharingguidelines⟩.
[41] L. Tang, Y. Kang, M. Shui, Unmodified α-$LiFe_5O_8$ as potential anode material of lithium ion battery and the revelation of conversion mechanism, J. Solid State Chem. 337 (2024) 124818, https://doi.org/10.1016/J.JSSC.2024.124818.
[42] A. Philip, A.R. Kumar, Synergism of carbonaceous additives in engineering of the supercapacitive performance of α-and λ-phases of manganese oxide, Electrochim. Acta 498 (2024) 144651, https://doi.org/10.1016/J.ELECTACTA.2024.144651.
[43] M.F. Iqbal, F. Nasir, F. Shabbir, Z.U.D. Babar, M.F. Saleem, K. Ullah, N. Sun, F. Ali, Supercapacitors: an emerging energy storage system, Adv. Energy Sustain. Res. (2025) 2400412, https://doi.org/10.1002/aesr.202400412.
[44] V. Augustyn, P. Simon, B. Dunn, Pseudocapacitive oxide materials for high-rate electrochemical energy storage, Energy Environ. Sci. 7 (2014) 1597–1614, https://doi.org/10.1039/c3ee44164d.
[45] T.C. Liu, W.G. Pell, B.E. Conway, S.L. Roberson, Behavior of molybdenum nitrides as materials for electrochemical capacitors: comparison with ruthenium oxide, J. Electrochem. Soc. 145 (1998) 1882–1888, https://doi.org/10.1149/1.1838571.
[46] P.S. Nanda, A. Gautam, A.K. Singh, R.S. Singh, Recent advances in rare earth doped metal oxide based nanomaterials for supercapacitors, J. Energy Storage 131 (2025) 117431, https://doi.org/10.1016/J.EST.2025.117431.
[47] S. Ardizzone, G. Fregonara, S. Trasatti, Inner" and "outer" active surface of RuO_2 electrodes, Electrochim. Acta 35 (1990) 263–267, https://doi.org/10.1016/0013-4686(90)85068-X.
[48] M.Z. Iqbal, M.M. Faisal, M. Sulman, S.R. Ali, A.M. Afzal, M.A. Kamran, T. Alharbi, Capacitive and diffusive contribution in strontium phosphide-polyaniline based supercapattery, J. Energy Storage 29 (2020) 101324, https://doi.org/10.1016/j.est.2020.101324.
[49] S.M. Mane, K.S. Wagh, A.M. Teli, S.A. Beknalkar, J.C. Shin, J. Lee, Mitigation of shape evolution and supercapacitive performance of $CuCo_2S_4$ electrodes prepared via a simple solvent variation approach, Appl. Sci. 13 (2023) 12122, https://doi.org/10.3390/app132212122.
[50] A. Lakshmi-Narayana, N. Attarzadeh, V. Shutthanandan, C.V. Ramana, High-performance $NiCo_2O_4$/graphene quantum dots for asymmetric and symmetric supercapacitors with enhanced energy efficiency, Adv. Funct. Mater. 34 (2024) 2316379, https://doi.org/10.1002/adfm.202316379.
[51] V. Kushwaha, K.D. Mandal, A. Gupta, P. Singh, $Ni_{0.5}Co_{0.5}S$ nano-chains: a high-performing intercalating pseudocapacitive electrode in asymmetric supercapacitor (ASC) mode for the development of large-scale energy storage devices, Dalton Trans. 53 (2024) 5435–5452, https://doi.org/10.1039/d3dt04184k.
[52] A. Scalia, F. Bella, A. Lamberti, C. Gerbaldi, E. Tresso, Innovative multipolymer electrolyte membrane designed by oxygen inhibited UV-crosslinking enables solid-state in plane integration of energy conversion and storage devices, Energy 166 (2019) 789–795, https://doi.org/10.1016/J.ENERGY.2018.10.162.
[53] A. Scalia, F. Bella, A. Lamberti, S. Bianco, C. Gerbaldi, E. Tresso, C.F. Pirri, A flexible and portable powerpack by solid-state supercapacitor and dye-sensitized solar cell integration, J. Power Sources 359 (2017) 311–321, https://doi.org/10.1016/J.JPOWSOUR.2017.05.072.
[54] D. Devadiga, M. Selvakumar, P. Shetty, M.S. Santosh, Recent progress in dye sensitized solar cell materials and photo-supercapacitors: a review, J. Power Sources 493 (2021) 229698, https://doi.org/10.1016/j.jpowsour.2021.229698.
[55] C. Tuc Altaf, A.M. Rostas, A. Popa, D. Toloman, M. Stefan, N. Demirci Sankir, M. Sankir, Recent advances in photochargeable integrated and all-in-one supercapacitor devices, ACS Omega 8 (2023) 47393–47411, https://doi.org/10.1021/acsomega.3c07464.